Journal Pre-proof

One-pot synthesis of Mn/Fe bimetal-doped metal-organic framework as multifunctional nanocarriers for esophageal cancer targeted therapy

Jia Ma, Xin Zhang, Xiangpeng Meng, Yuhang Dai, Huaiyong Wang, Milad Ashrafizadeh, João Conde, Zhenggang Li, Enyang Yao, Wei He

PII: S2095-1779(26)00072-9

DOI: https://doi.org/10.1016/j.jpha.2026.101617

Reference: JPHA 101617

To appear in: *Journal of Pharmaceutical Analysis*

Received Date: 25 March 2025

Revised Date: 24 March 2026

Accepted Date: 26 March 2026

Please cite this article as: J. Ma, X. Zhang, X. Meng, Y. Dai, H. Wang, M. Ashrafizadeh, J. Conde, Z. Li, E. Yao, W. He, One-pot synthesis of Mn/Fe bimetal-doped metal-organic framework as multifunctional nanocarriers for esophageal cancer targeted therapy, *Journal of Pharmaceutical Analysis*, https://doi.org/10.1016/j.jpha.2026.101617.

One-pot synthesis of Mn/Fe bimetal-doped MOF as multifunctional nanocarriers for esophageal cancer targeted therapy

Running title: UA/siMTH1@MnFe-MOF@HA for esophageal cancer treatment

Jia Ma[1#], Xin Zhang[2#], Xiangpeng Meng[2#], Yuhang Dai[3], Huaiyong Wang[3], Milad Ashrafizadeh[4], João Conde[5****], Zhenggang Li[6***], Enyang Yao[7**], Wei He[3*]

[1]Department of Gastroenterology, The Fourth Affiliated Hospital of China Medical University, Shenyang, 110032, Liaoning, China

[2]Department of General Surgery, The Shengjing Hospital of China Medical University, Shenyang, 110004, China

[3]Department of Thoracic Surgery, The Shengjing Hospital of China Medical University, Shenyang, 110004, China

[4]Department of Radiation Oncology, Shandong Cancer Hospital and Institute, Shandong First Medical University and Shandong Academy of Medical Sciences, Jinan, 250000, China

[5]Comprehensive Health Research Centre, NOVA Medical School, Faculdade de Ciências Médicas, NMS, FCM, Universidade Nova de Lisboa, Lisboa, 1169, Portugal

[6]Department of Anesthesiology, The Shengjing Hospital of China Medical University, Shenyang, 110004, China

[7]Department of Orthopedics, The Shengjing Hospital of China Medical University, Shenyang, 110004, China

[#]These authors contributed equally to this work.

***Corresponding authors:**

Wei He, hewei@sj-hospital.org; Enyang Yao, yaoenyang@sj-hospital.org; Zhenggang Li, Lzgxyh12@sj-hospital.org; João Conde, joao.conde@nms.unl.pt

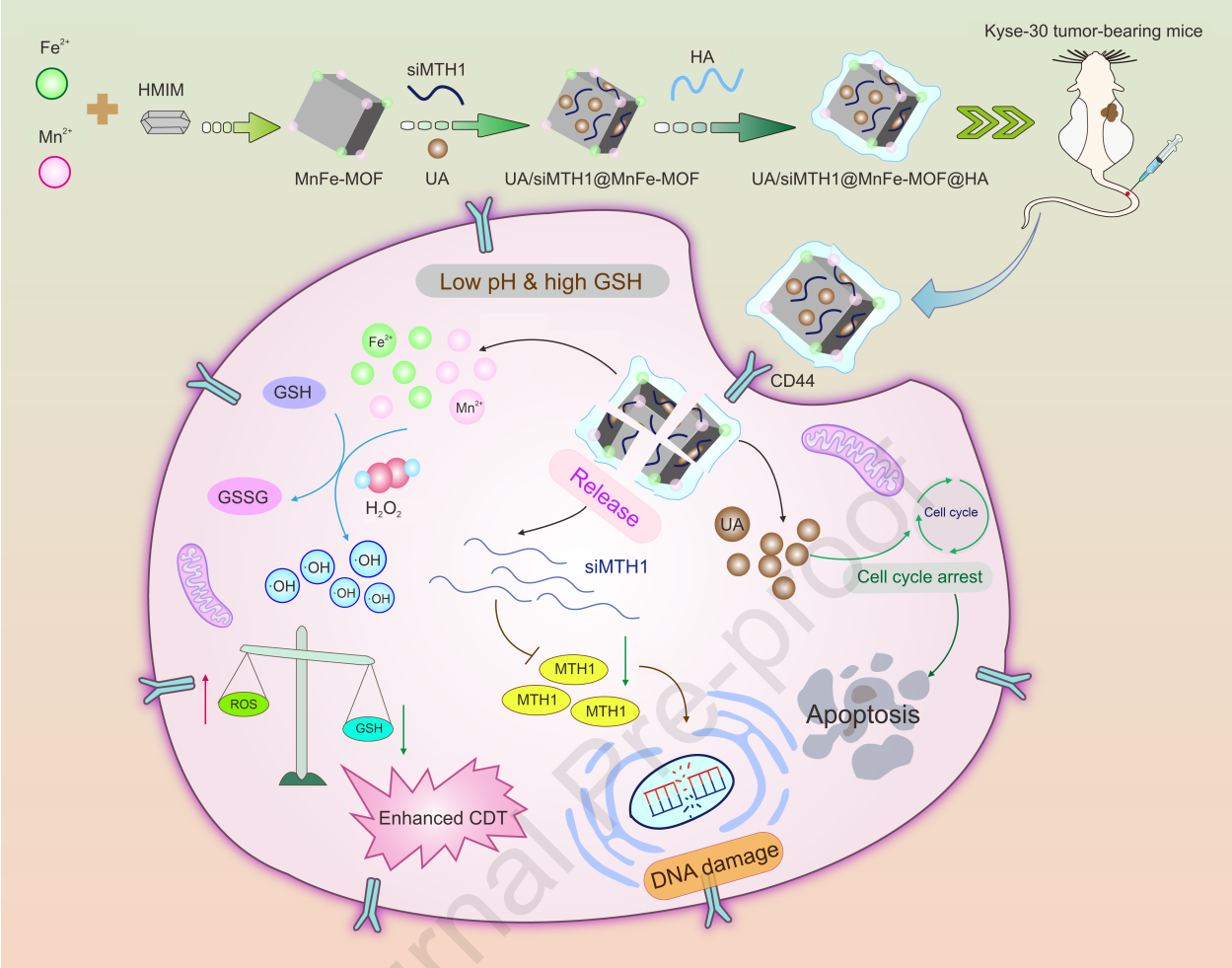

One-pot synthesis of Mn/Fe bimetal-doped metal-organic framework as multifunctional nanocarriers for esophageal cancer targeted therapy

Abstract

Chemodynamic therapy (CDT) offers new opportunities to eliminate cancer by killing tumor cells through the production of toxic hydroxyl radicals (·OH) in the tumor region. However, the efficiency of CDT is severely hampered by insufficient levels of hydrogen peroxide and large amounts of glutathione (GSH) in tumor cells. To address this issue, we developed Mn/Fe bimetallic metal-organic framework (MnFe-MOF) nanocarriers that could intelligently respond to the tumor microenvironment for loading ursolic acid (UA) and siMTH1, followed by surface modification with hyaluronic acid (HA). Finally, a nanoparticle named UA/siMTH1@MnFe-MOF@HA was developed for the treatment of esophageal cancer. Benefiting from HA-coated encapsulation, UA/siMTH1@MnFe-MOF@HA achieved Kyse-30 cell targeting and slow release of UA/siMTH1. The Mn/Fe ions doped in the nanoframework catalyzed the Fenton reaction in the tumor microenvironment with acidic pH and overexpression of GSH to promote reactive oxygen species (ROS) eruption, and further amplified oxidative stress by consuming GSH, resulting in cell damage. Moreover, siMTH1 released by the nanoparticles can cause DNA damage and induce cellular senescence to kill cancer cells, while the released UA can induce G1 cell cycle arrest to inhibit cell proliferation, synergistically enhancing the therapeutic effect. UA/siMTH1@MnFe-MOF@HA exhibited outstanding tumor suppression *in vitro* and *in vivo*, with negligible systemic toxicity. This transition metal-doped multifunctional MOF enabled efficient CDT and provides a promising paradigm for esophageal cancer therapy.

Keywords: Chemodynamic therapy; metal ion; nanoparticle; esophageal cancer

1. Introduction

Esophageal cancer is a common malignant tumor worldwide and ranks 7th among cancer-related causes of death [1]. The incidence of esophageal cancer has increased dramatically in recent years. Although conventional and neoadjuvant modalities have boosted the overall survival of patients with esophageal cancer, the long-term prognosis remains dismal, with an estimated 5-year survival rate of nearly 20% [2]. The main reasons for treatment failure are tumor metastasis and recurrence [3]. Therefore, the development of new therapeutic strategies, especially precision medicine, is essential for improving clinical practice.

Ursolic acid (UA) is a natural pentacyclic triterpene widely found in vegetables, fruits, and herbs [4]. It possesses

multiple pharmaceutical properties, including antioxidant, anti-inflammatory, and antibacterial effects [5–7]. These safety and pleiotropic features of UA emphasize its potential in cancer therapy [8]. Multiple studies have shown that UA can regulate the proliferation, apoptosis, metastasis, and angiogenesis of cancer cells through various mechanisms and signaling pathways, thereby inhibiting cancer formation and progression [9,10]. The anticancer effects of UA have been reported in various types of cancer, including esophageal cancer. Although UA is a promising anticancer bioactive molecule, there are still many hurdles to overcome before it can be applied in the clinic. On the one hand, the low solubility and low permeability of UA limit its bioavailability and pharmacokinetics, thus reducing its effectiveness [11]. However, the non-specific distribution of UA in the body and possible hepatocytotoxicity caused by long-term overdose limit its use [12,13]. To address these issues, researchers have developed novel strategies to modify the structure of UA using nanodelivery systems to improve its pharmacokinetic properties, thereby increasing its anticancer activity and reducing adverse reactions [14].

Furthermore, the emergence of novel therapeutic modalities, such as targeted therapy, has greatly improved the quality of life of patients with cancer [15]. However, the development of targeted therapy for esophageal cancer lags behind that for other solid tumors, and the available therapeutic targets are limited [16]. Therefore, the search for better therapeutic targets is urgent. Oxidative stress is an important hallmark of cancer pathogenesis. The resulting redox imbalance can induce DNA damage and genomic instability, thereby forming low or medium levels of reactive oxygen species (ROS) signaling to promote cancer cell survival [17]. Notably, excess ROS can trigger tumor suppression by damaging the DNA of cancer cells [18]. In this process, cancer cells activate their antioxidant defenses to combat DNA damage and enhance their tolerance to high ROS levels, mainly by upregulating DNA repair proteins such as human MutT Homolog 1 (MTH1) [19]. Importantly, the toxic effect of MTH1 in reducing ROS is only present in tumor cells and is rare in normal cells [20]. This property makes it an attractive target for cancer therapies. MTH1 overexpression is a marker of poor prognosis in patients with esophageal cancer and could be a potential target for cancer therapy [21]. Recently, Raj et al. [22] found that MTH1 expression in HeLa cells was significantly downregulated using small interfering RNA (siRNA) and showed the effect of enhanced chemodynamic therapy (CDT). However, the targeted inhibition of MTH1 in esophageal cancer therapy has rarely been reported.

Inspired by these reports, we designed a nano-delivery system for piggybacking UA and MTH1 siRNA (siMTH1) to realize the synergistic therapeutic effects of drugs and molecular targets. Here, we chose the Mn/Fe bimetallic metal-organic framework (MnFe-MOF) as the delivery carrier for the drug. Compared with conventional MOF, metal-doped MnFe-MOFs have higher catalytic activity and material stability, exhibiting excellent electrochemical properties [23]. To improve the biocompatibility of the nanoparticles and prolong the *in vivo* circulation time, we employed a hyaluronic acid

(HA) encapsulation strategy to synthesize UA/siMTH1@MnFe-MOF@HA nanomedicine. In various tumor lesions, HA-specific receptors, especially the CD44 receptor, which is highly expressed on the surface of tumor cells, can specifically bind to HA and achieve tumor targeting through the receptor-ligand mechanism [24]. Meanwhile, HA can be degraded by high concentration of hyaluronidase in tumor cells [25]. Therefore, these unique properties make HA a promising nanocarrier in the research of anti-tumor drug delivery. We confirmed that these nanoparticles possessed the active targeting ability of cancer cells and showed excellent effects in inhibiting esophageal cancer by generating excess ROS and causing DNA damage (**Scheme 1**).

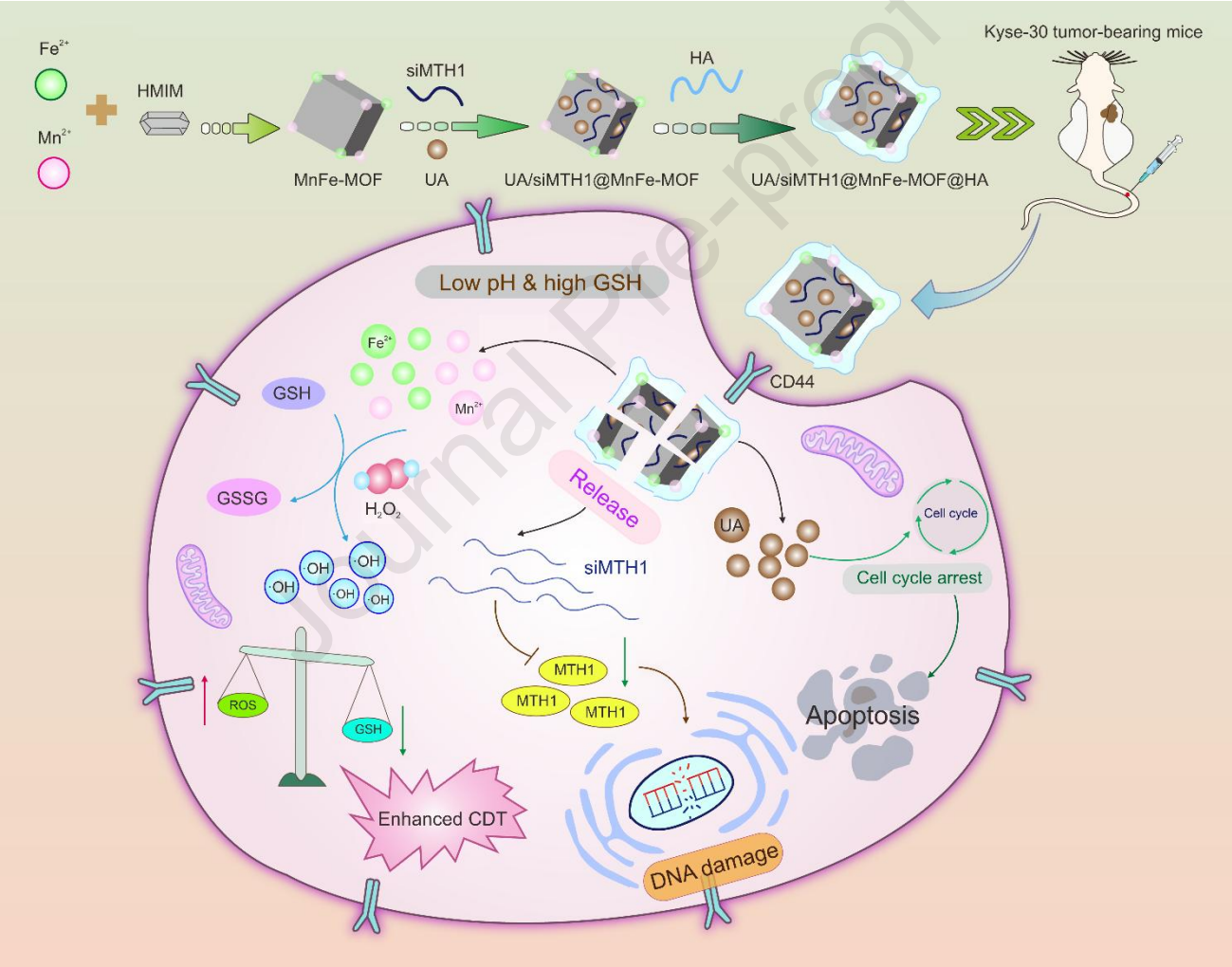

Scheme 1. Schematic illustration of synthetic ursolic acid (UA)/ human MutT Homolog 1 small interfering RNA (siMTH1)@ Mn-Fe bimetallic metal-organic framework (MnFe-MOF)@ hyaluronic acid (HA) for targeted delivery to esophageal cancer cells and reveals its potential to exert a synergistic effect of chemodynamic and gene therapy in esophageal cancer therapy. HMIM: 2-methylimidazole; GSH: glutathione; GSSG: glutathione disulfide; H_2O_2: hydrogen peroxide; OH: hydroxyl radical; ROS: reactive oxygen species; CDT: chemodynamic therapy; CD44: cluster of differentiation-44.

2. Materials and methods

2.1 Materials

$Mn(NO_3)_2$, N-Hydroxysuccinimide (NHS), 1,2-Dichloroethane (EDC), and HA were purchased from Shanghai Macklin Biochemical Technology Co., Ltd. (Shanghai, China). 2-methylimidazole (HMIM) and dimethylformamide (DMF) were purchased from Shanghai Yuanye Bio-Technology Co., Ltd. (Shanghai, China). $(NH_4)_2Fe(SO_4)_2$, UA, and dimethyl sulfoxide (DMSO) were obtained from Beijing Solarbio Science & Technology Co., Ltd. (Beijing, China). The Cell Counting Kit-8 (CCK-8) assay kit, hematoxylin-eosin (H&E) staining kit, terminal deoxynucleotidyl transferase dUTP nick end labeling (TUNEL) assay kit, Annexin V-fluorescein isothiocyanate (FITC) apoptosis assay kit, cell cycle analysis kit, senescence-associated-beta-galactosidase (SA-β-gal) staining kit, ROS assay kit, glutathione (GSH) kit, and GSH/ glutathione disulfide (GSSG) assay kit were obtained from Beyotime Biotechnology (Shanghai, China).

2.2 Cell culture

Esophageal squamous cell carcinoma cell line (Kyse-30 cells, purchased from Wuhan Pricella Biotechnology Co., Ltd., Wuhan, China) and esophageal epithelial cell line (HEEC, purchased from Shanghai Yu Bo Biotech Co., Ltd., Shanghai, China) were inoculated with Roswell Park Memorial Institute-1640 supplemented with 10% fetal bovine serum (FBS) and 1% penicillin-streptomycin, followed by incubation in a 37 °C incubator containing 5% CO_2.

2.3 Synthesis of UA/siMTH1@MnFe-MOF@HA nanosystem

First, $Mn(NO_3)_2$ (11 mmol/L), HMIM (0.28 g), and $(NH_4)_2Fe(SO_4)_2$ (100 μmol/L) were dissolved in DMF (10 mL) and stirred evenly. The mixture was then heated to 130 °C and reacted for 5 min. After centrifugation at 9000 rpm for 20 min, the nanomaterial MnFe-MOF was obtained and dried.

Second, MnFe-MOF (10 mg/mL) dissolved in deionized water was preactivated with EDC/NHS (pH 5.6, 5 mg/mL) at 37 °C for 2 h, followed by loading of the drugs (UA, siMTH1, or UA + siMTH1) into MnFe-MOF by adsorption. For example, MnFe-MOF, UA (30 mg/mL), and siMTH1 (5 μmol) were mixed in DMSO and stirred continuously for 12 h. The mixture was then centrifuged at 10000 rpm for 10 min and washed three times with DMSO to obtain UA/siMTH1-loaded MnFe-MOF nanoparticles (UA/siMTH1@MnFe-MOF). The same method was used to load the other individual drugs. The siMTH1 sequences were designed at the Designer of Small Interfering RNA website, with the sense strand 5'-UGCACUUUGCCCCCAAAGCCA-3 and the antisense strand 5'-GCUUUGGGGGCAAAGUGCAAG-3'. In addition, to preliminarily verify the optimal UA@MnFe-MOF and siMTH1 ratio, the siRNA encapsulation rate of siMTH1 (labeled by 5-Carboxyfluorescein (FAM)): UA@MnFe-MOF with different weight ratios (1:1, 1:5, 1:10, or 1:15) was explored

using fluorescence spectroscopy. Pure siMTH1 was used as the negative control.

Finally, to improve the targeting properties of the nanoparticles and prolong the circulation time of the drug *in vivo*, the surface of the nanoparticles was modified using HA. MnFe-MOF loaded or unloaded with drugs was dissolved in deionized water. Then, a DMSO solution containing HA (40 μg/mL) was added and stirred for 12 h. The mixture was centrifuged at 10000 rpm for 10 min to obtain the precipitate, which was washed three times with DMSO, and the HA-coated nanoparticles were harvested, including MnFe-MOF@HA, UA@MnFe-MOF@HA, siMTH1@MnFe-MOF@HA, and UA/siMTH1@MnFe-MOF@HA.

2.4 Characterization of nanoparticles

The morphology of the nanoparticles was characterized using transmission electron microscopy (TEM). The average particle size and zeta potential of the nanoparticles were measured using a laser particle size (Microtrac MRB, Shanghai, China) and zeta potential analyzer (BeNano 180 Zeta Pro, Dandong, Liaoning, China), respectively. The major elemental species in UA/siMTH1@MnFe-MOF@HA were detected using X-ray spectroscopy (EDX) mapping. To further confirm the elemental composition in nanomaterials, we used X-ray photoelectron spectroscopy (XPS) and inductively coupled plasma-optical emission spectrometry (ICP-OES, ICPOES730, Beijing, China) to determine the chemical component and content in UA/siMTH1@MnFe-MOF@HA. We also confirmed the success of drug piggybacking and HA modification in UA/siMTH1@MnFe-MOF@HA nanoparticles through a series of experiments. For instance, the characteristic peaks of siRNA were evaluated using fluorescence spectroscopy, MnFe-MOF, UA, and HA were characterized using Fourier-transform infrared spectroscopy (FTIR, Spectrum 1000, Perkin-Elmer, Waltham, MA, USA), and the crystal structure of MnFe-MOF was observed using X-ray diffraction (XRD, D8 Advance, Bruker, Beijing, China).

2.5 Evaluation of stability, drug loading, and drug release behavior

To reveal the biocompatibility of UA/siMTH1@MnFe-MOF@HA nanoparticles, we performed a stability study. In brief, UA/siMTH1@MnFe-MOF@HA was dissolved in phosphate-buffered saline (PBS) or 10% FBS, and the average particle size and polydispersity index of the nanoparticles at specific time points were determined by dynamic light scattering. In addition, the ultraviolet (UV) spectrophotometer (U-2910, Thermo Fisher Scientific, Waltham, MA, USA) was used to determine the drug loading and encapsulation rate of UA in UA/siMTH1@MnFe-MOF@HA. First, the UA mother liquor was prepared and diluted to obtain standard curves at different concentrations. Next, UA/siMTH1@MnFe-MOF@HA was dissolved in deionized water and centrifuged at 12000 rpm for 10 min to collect the supernatant. After 10-fold dilution, the absorbance of the sample at 220 nm was determined, and the concentration of UA was calculated

according to the standard curve. Moreover, fluorescence spectroscopy was utilized to evaluate the drug loading of siMTH1 (labeled by FAM) in UA/siMTH1@MnFe-MOF@HA. The acid and GSH sensitivity of nanoparticles can be used to control drug release in the tumor microenvironment (low pH and overexpressed GSH), playing a positive role in targeted cancer therapy [26]. Hence, we evaluated the pH and GSH responsiveness of the nanosystem using dialysis experiments. The UA/siMTH1@MnFe-MOF@HA (FAM-labeled siMTH1) nanoparticles were dispersed in dialysis bags containing PBS (2 mL) at different pH values (5.5 and 7.4). Moreover, UA/siMTH1@MnFe-MOF@HA (FAM-labeled siMTH1) nanoparticles were dispersed in PBS without or with GSH (10 mM). Subsequently, the dialysis bags were immersed in bottles containing PBS (20 mL) at 37 °C in the dark. The dialysate (1 mL) was collected at given time intervals, and its UV-visible absorption or fluorescence spectra (excitation wavelength, 480 nm; emission wavelength, 520 nm) were measured. *In vitro* degradation experiments were performed by dispersing UA/siMTH1@MnFe-MOF@HA in solutions of different pH (5.5 or 7.4), and 20 μL of the solution was taken at specific time points (6 h and 12 h) for TEM and energy dispersive spectroscopy (EDS) observations.

2.6 Assessment of GSH depletion capability

Different concentrations of MnFe-MOF@HA or UA/siMTH1@MnFe-MOF@HA (1 mL) were mixed with GSH (1 mL, 10 mM) and reacted in a shaker for 2 h at 100 rpm, 37 °C. The mixture was centrifuged at 10000 rpm for 5 min, and the supernatant (1 mL) was collected, followed by the addition of 5,5'-dithiobis-(2-nitrobenzoic acid) solution (1 mL, 5 mM). After the reaction for 1 h, the absorbance at 412 nm was measured, and the consumption of GSH was calculated.

2.7 Detection of hydroxyl radical (·OH)

Next, 5 μL of MnFe-MOF@HA or UA/siMTH1@MnFe-MOF@HA was added to a centrifuge tube, and 2.5 mL of deionized water was Then, 10 μL of hydrogen peroxide (H_2O_2, mass concentration of 5%) and 25 μL of TMB were added to the mixture. After incubation for 30 min, the intensity of the absorption peak at 450 nm was measured to reflect the formation of ·OH.

2.8 Assay of in vitro cytocompatibility

The safety of nanomaterials is the basis of clinical transformation of nanomedicine; thus, we first evaluated the *in vitro* cytotoxicity of nanomaterials. Kyse-30 and HEEC cells were inoculated in 96-well plates at a density of 2000 cells/well and then treated with different concentrations of MnFe-MOF or MnFe-MOF@HA for 24 h in an incubator (37 °C and 5% CO_2). CCK-8 solution (10 μL) was added to each well, and incubation was continued for 2 h. The absorbance at

450 nm was measured using an enzyme meter. The biocompatibility of UA/siMTH1@MnFe-MOF@HA with erythrocytes was further assessed by hemolysis analysis. Erythrocyte suspensions (100 μL) were added to PBS buffer (negative group), deionized water (positive group), or UA/SiMTH1@MnFe-MOF@HA dispersion at concentrations of 6.25 μg/mL, 12.5 μg/mL, 25 μg/mL, 50 μg/mL, 100 μg/mL, or 200 μg/mL. After 12 h, the mixtures were centrifuged, and the absorbance of the supernatants of each group was measured at 541 nm. The hemolysis rate was calculated based on previous report [27].

In addition, to explore the *in vitro* antitumor effect of nanoparticles, we determined the optimal concentration of UA/siMTH1@MnFe-MOF@HA for treating Kyse-30 cells. Briefly, Kyse-30 cells were inoculated into 96-well plates and treated with different concentrations of UA/siMTH1@MnFe-MOF@HA for 24 h. Next, cell viability was measured using the CCK-8 method, and the half maximal inhibitory concentration (IC_{50}) value was calculated.

2.9 Evaluation of cellular uptake ability of UA/siMTH1@MnFe-MOF@HA

The cellular internalization efficiency of the UA/siMTH1@MnFe-MOF@HA nanoparticles was evaluated in Kyse-30 cells using flow cytometry. Kyse-30 cells were inoculated into 6-well plates (5×10^5 cells/well) and cultured in an incubator for 24 h. Subsequently, FITC-modified UA/siMTH1@MnFe-MOF or UA/siMTH1@MnFe-MOF@HA was added to the Kyse-30 cells, and samples were collected after treatment for 2, 4, and 6 h, respectively. As a control, we also observed the uptake of nanoparticles by normal cell HEEC. The cellular uptake capacity was assessed using confocal laser scanning microscopy (CLSM). Briefly, the collected cells were washed with PBS, fixed with ethanol, and stained with 4',6-diamidino-2-phenylindole (DAPI). Next, the tumor-targeted cell distribution and endocytosis behavior of the nanosystem were observed using an inverted fluorescence microscope.

2.10 Detection of cell apoptosis

Kyse-30 cells were inoculated in 12-well plates and treated with different formulations for 24 h, including PBS, MnFe-MOF@HA, free UA, UA@MnFe-MOF@HA, and UA/siMTH1@MnFe-MOF@HA. Cells from each group were collected, digested with trypsin, resuspended in PBS, and centrifuged at 1,500 rpm for 5 min. After resuspension, the precipitates were stained with Annexin V-FITC and propidium iodide (PI) reagents and incubated at room temperature for 25 min in the dark. Cell samples were analyzed by flow cytometry, and apoptosis data were quantified using CELL Quest software.

2.11 Measurement of live/dead cells

Kyse-30 cells were cultured in 96-well plates and treated with the same formula as described above. After incubation for 24 h, all cell samples were collected, centrifuged, and resuspended for further processing. Afterwards, the cells were

stained with Calcein AM/PI for 15 min, and dead (red fluorescence)/live cells (green fluorescence) were observed under a fluorescence microscope.

2.12 Evaluation of cell cycle

Kyse-30 cells were seeded in 12-well plates and allowed to adhere overnight. The following day, the cells were treated with different drugs or PBS for 24 h. Subsequently, the cells were fixed with 70% ethanol and stained with propidium iodide (0.5 mL). After incubation in the dark for 30 min, the cell cycle was analyzed by flow cytometry.

2.13 Detection of ROS level and intracellular GSH content

Kyse-30 cells were inoculated in 12-well plates and treated with different formulations for 24 h. Cells from each group were collected and washed with PBS. ROS-positive cells and nuclei were stained with 2′,7′-dichlorodihydrofluorescein diacetate (DCFH-DA) and DAPI, respectively, and incubated at 37 °C for 20 min. The cells were then washed three times with serum-free culture medium, and the ROS levels were observed using CLSM and flow cytometry. Subsequently, the GSH consumption capacity of the nanoparticles was assessed within the cells. After collecting the cells from different treatment groups, they were washed twice with PBS and centrifuged at 8,000 rpm for 10 min. GSH and GSH/GSSG content in the supernatant was determined according to the protocol recommended by the manufacturer.

2.14 Assay of SA-β-gal activity

Kyse-30 cells were inoculated in 6-well plates and treated with different protocols for 24 h, followed by cell collection. The samples were fixed with 0.2% glutaraldehyde for 15 min at room temperature and then stained with β-galactosidase overnight at 37 °C. SA-β-gal-positive cells were counted using a light microscope.

2.15 Western blot assay

Kyse-30 cells were treated with different formulations for 24 h and then harvested. Protein lysate (50 μL) was added to the cell samples from each group, and the protein concentration of the samples was determined using the BCA assay. The protein samples were then separated by sodium dodecyl sulphate polyacrylamide gel electrophoresis and transferred to polyvinylidene fluoride (PVDF) membranes. These membranes were incubated with primary antibodies (gammaH2AX (γH2AX, No.7631, CST, Danvers, MA, USA), transforming growth factor beta (TGF-β) (No.SAB4502958, MECK, Shanghai, China), phosphorylated Retinoblastoma protein (p-Rb) (No.ab184796, Abcam, Cambridge, MA, US), p21 (No.2947, CST), MTH1 (No.3716, CST), glyceraldehyde 3-phosphate dehydrogenase (GAPDH) (No.ab181602, Abcam,

Cambridge, MA, USA) overnight at 4 °C and reacted with secondary antibodies (goat anti-Rabbit IgG, No.A0208, Beyotime, Shanghai, China) for 1 h. Afterwards, these bands were colored with chemiluminescent reagent, and the optical density on the membrane was quantified using ImageJ software. GAPDH was used as an internal reference. For MTH1 detection, we also set up free siMTH1, siMTH1@MnFe-MOF, and siMTH1@MnFe-MOF@HA treatment groups.

2.16 Reverse transcription quantitative polymerase chain reaction (RT-qPCR) analysis

Kyse-30 cells were cultured in 6-well plates (2×10^5 cells/well) and incubated with PBS, free siMTH1, siMTH1@MnFe-MOF, siMTH1@MnFe-MOF@HA, or UA/siMTH1@MnFe-MOF@HA for 24 h. Total RNA was extracted from each group using TRIzol, and reverse transcription was performed. Next, the messenger RNA (mRNA) level of MTH1 was quantified by RT-qPCR using a PCR instrument (CFX96Touch, Bio-Rad, Hercules, CA, USA). GAPDH was used as the housekeeping gene for normalization, and the relative expression of the gene was calculated using the conventional $2^{-\triangle\triangle Ct}$ method. The primer sequences used are as follows: MTH1 (103 bp), forward: 5'-AGGCTCTATACCCTGGTGCT-3', reverse: 5'-CTTTGCCCCCAAAGCCATTC-3'; GAPDH (236 bp), forward: 5'-AGCTTCAGCCCCAGGAAATC-3', reverse: 5'-GACATACTGCTGGGCCAGTT-3'. In addition, we explored the stability of the nanoparticle knockdown gene. Briefly, Kyse-30 cells were cultured in 6-well plates, treated with UA/siMTH1@MnFe-MOF@HA for 24 h, and collected. Treated cells were also collected after three consecutive passages. The mRNA levels of MTH1 before and after passaging cultures were examined using RT-qPCR.

2.17 Establishment of the esophageal cancer model

The 4-week-old male BALB/c nude mice were purchased from the Experimental Animal Center of Yangzhou University. All mice were acclimated for one week before the formal experiments. Animal experiments were performed following the protocol approved by the Ethics Committee of Yangzhou University (Approval No.: 202407035). Kyse-30 cells (3×10^6) were suspended in PBS (100 μL) and injected subcutaneously into the right axilla of mice to establish an esophageal tumor model. When the tumor volume reached 100 mm^3, the mice were randomly grouped for the animal experiments.

2.18 In vivo biodistribution imaging of nanoparticles

Tumor-bearing mice were divided into UA/siMTH1@MnFe-MOF and UA/siMTH1@MnFe-MOF@HA groups, with 6 mice in each group. Cy5.5-labeled nanoparticles (20 kg/mg) were injected into the mice through the tail vein. At specific time points, the mice were anesthetized and observed using an *in vivo* visible light imaging system (Caliper Life Sciences,

Hopkinton, MA, USA). After 48 h after nanomedicine injection, the mice were euthanized, and the major organs were collected for *ex vivo* imaging, followed by calculation of the fluorescence intensity of each organ.

2.19 In vivo antitumor experiments

Tumor-bearing mice were randomly divided into five groups: control, MnFe-MOF@HA, UA, UA@MnFe-MOF@HA, and UA/siMTH1@MnFe-MOF@HA ($n = 6$). The mice received daily tail vein injections of saline, UA alone, or nanoparticles (20 mg/kg). Tumor volumes and body weights of mice were recorded every other day, and the mice were euthanized after 14 days of treatment. Blood samples were collected before execution and centrifuged to obtain plasma. Next, the major organs and tumor tissues of the mice were collected for subsequent analysis. Tumor tissues were assayed using RT-qPCR and western blot experiments to detect the mRNA and protein expression levels of MTH1. In addition, the tumor or organ tissues were fixed with 4% paraformaldehyde, dehydrated/transparent with ethanol, and paraffin-embedded to prepare frozen sections. TUNEL staining, immunohistochemical staining (Ki67, TGF-β, p-Rb, p21), γH2AX immunofluorescence staining, and SA-β-gal staining were performed on the tumor sections to evaluate the pathological status of the tissues, respectively.

2.20 In vivo biocompatibility assay

To evaluate the biosafety of the nanoparticles, we also conducted HE staining on tissue sections of the major organs to observe whether there was any damage to the organs. Moreover, the content of alanine aminotransferase (ALT), aspartate aminotransferase (AST), creatinine (CRE), and Urea in the serum of mice were measured by an automatic biochemical analyzer (Cobas c-311, Roche, Basel, Switzerland) to evaluate the toxicity of the drug on the liver and kidney functions of tumor-bearing mice.

2.21 Statistical analysis

Data are presented as mean ± standard deviation (SD), and differences between groups were compared using Student's *t*-test or one-way analysis of variance (ANOVA). All statistics were completed on GraphPad (version 7.0), with statistical significance denoted by $^{*}P < 0.05$ and $^{**}P < 0.01$.

3. Results

3.1 Preparation and characterization of UA/siMTH1@MnFe-MOF@HA

In this study, MnFe-MOF nanoparticles were synthesized using a one-pot hydrothermal method. Subsequently, the

therapeutic drugs (UA and siMTH1) were loaded onto MnFe-MOF, and the nanoparticles were modified with HA to obtain UA/siMTH1@MnFe-MOF@HA. The specific synthesis process is shown in **Fig. 1A**. Notably, fluorescence detection confirmed that the encapsulation rate of siMTH1 reached a maximum when the weight ratio of siMTH1:MnFe-MOF was 1:5, which was approximately 80% (**Fig. 1B**). Hence, this ratio was selected for the preparation of the nanoparticles. TEM revealed that MnFe-MOF exhibited a clear tetrahedral shape without significant aggregation. After HA encapsulation, a thin film appeared on the surface of the nanoparticles (MnFe-MOF@HA), and the loading of UA/siMTH1 did not affect the morphology of the nanoparticles (**Fig. 1C**). The particle size detection analysis showed that the average sizes of MnFe-MOF, MnFe-MOF@HA, and UA/siMTH1@MnFe-MOF@HA were 170.2 nm, 185.5 nm, and 190.8 nm, respectively (**Fig. 1D**). The measured zeta potentials of MnFe-MOF and Mn-Fe-MOF@HA were 3.3 ± 0.5 mV and −9 ± 0.82 mV, respectively. After the addition of siMTH1 and UA, the zeta potential of UA/siMTH1@MnFe-MOF@HA decreased to –18.3 ± 1.25 mV (**Fig. 1E**). Next, the fluorescence spectrogram of siMTH1 was observed in UA/siMTH1@MnFe-MOF@HA (**Fig. 1F**). The nanoframework equipped with metal ions could effectively generate •OH, and the prepared UA/siMTH1@MnFe-MOF@HA could further enhance the •OH generation (**Fig. 1G**), which may be attributed to the reduction ability of UA to metal ions. This creates conditions for the Fenton reaction to occur. Subsequently, the functional groups of the nanoparticles were qualitatively analyzed using FTIR (**Fig. 1H**). For MnFe-MOF@HA, normal absorption peaks were observed at 1382cm^{-1}, 1578cm^{-1}, and 1703cm^{-1}, which were caused by the irregular stretching vibration of C = O. Vibration absorption occurred at 748cm^{-1} and 549cm^{-1}, which belonged to the characteristic peaks of metallic oxygen (Fe-O). These findings confirmed the successful synthesis of the MnFe-MOF material. In addition, amide band, and ·OH group peaks were observed at 1612 cm^{-1} and 3200–3600 cm^{-1}, respectively, indicating the presence of HA. The characteristic peak of UA was located at 2872 cm^{-1}, corresponding to the methyl group. In the spectrum of UA@MnFe-MOF@HA, we observed peaks formed by the superposition of the infrared spectra of MnFe-MOF@HA and free UA, that is, all the above major functional groups were retained, but the peak intensity was slightly reduced. These results indicate that UA was successfully coupled to MnFe-MOF@HA. Elemental mapping showed that Fe, Mn, C, O, and N were uniformly distributed on the particles, further indicating the successful preparation of UA/siMTH1@MnFe-MOF@HA (**Fig. 1I**). ICP-OES analysis revealed that the actual Fe and Mn contents in UA/siMTH1@MnFe-MOF@HA were 3 wt% and 7 wt%, respectively (**Fig. 1J**). Besides, the XPS spectra of the Fe 2p region showed that the peaks at 711.6 ev and 713.3 ev belong to Fe^{2+} and Fe^{3+}, respectively (**Fig. 1K**). In the Mn 2p region, 639.5 ev and 642.5 ev were associated with Mn^{2+} and Mn^{4+}, respectively (**Fig. 1L**). We also found that the proportions of Fe^{2+}, Fe^{3+}, Mn^{2+}, and Mn^{4+} in UA/siMTH1@MnFe-MOF@HA were 35.21%, 30.77%, 42.04%, and 38.72%. These data further verified the successful introduction of Fe and Mn ions into MOF composite nanoparticles. The crystal structures of the prepared nanoparticles

were assessed using XRD (**Fig. 1M**). In the MnFe-MOF material, strong and sharp peaks were observed at 9.17°, 9.81°, 16.53°, 25.41°, and 33.05°, confirming the presence of the highly crystalline product MIL-101 (Fe). The XRD profile was consistent with a previous report [28]. Although the final synthesized nanoparticles (UA/siMTH1@MnFe-MOF@HA) retained the original characteristic signals, the intensity of the peaks was significantly reduced. This decrease in the crystallinity of the nanoparticles may be due to HA encapsulation. Notably, there was no significant change in the particle size of UA/siMTH1@MnFe-MOF@HA in PBS or 10% FBS solution during the one-week storage period (6.5 days), indicating good physical stability and dispersion (**Fig. 1N**). In addition, we observed that the loading rate of UA and siMTH1 in UA/siMTH1@MnFe-MOF@HA was approximately 25.57% and 12%, respectively.

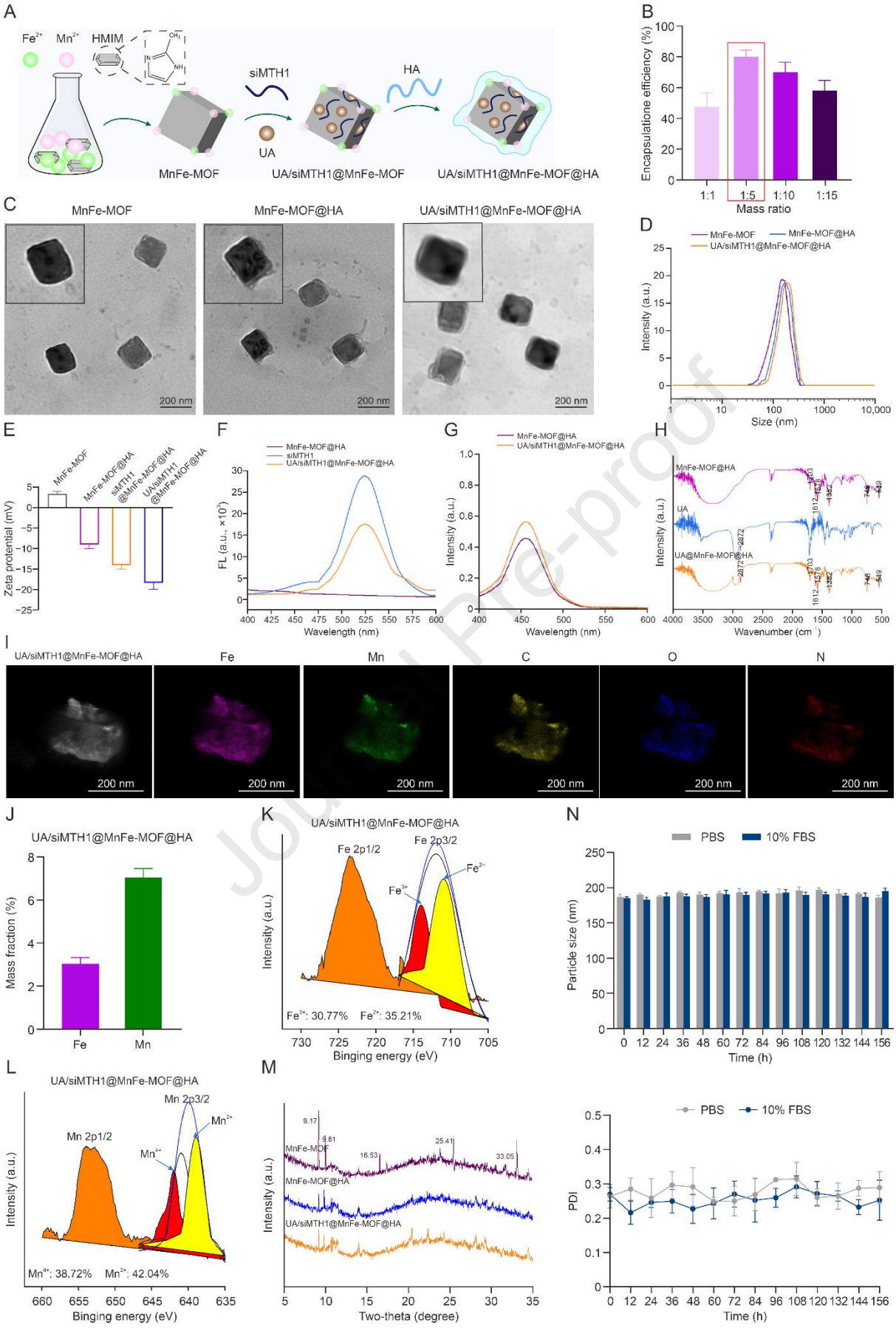

Figure 1. Synthesis and characterization of ursolic acid (UA)/ human MutT Homolog 1 small interfering RNA (siMTH1)@

Mn-Fe bimetallic metal-organic framework (MnFe-MOF)@ hyaluronic acid (HA) nanoparticles. (A) Schematic diagram of the preparation process of UA/siMTH1@MnFe-MOF@HA. (B) Spectrophotometric assessment of small interfering RNA (siRNA) encapsulation rate (siMTH1: UA@MnFe-MOF from 1:1 to 1:15). (C) Transmission electron microscopy (TEM) images of MnFe-MOF, MnFe-MOF@HA, and UA/siMTH1@MnFe-MOF@HA. (D) The particle size distribution of MnFe-MOF, MnFe-MOF@HA, and UA/siMTH1@MnFe-MOF@HA. (E) Zeta potential of nanoparticles. (F) Fluorescence spectrogram of MnFe-MOF@HA, siMTH1, and UA/siMTH1@MnFe-MOF@HA to confirm the load of siMTH1. (G) Ultraviolet-visible (UV-vis) spectra of hydroxyl radicals (·OH) generation. (H) Fourier-transform infrared spectroscopy (FTIR) spectra of MnFe-MOF@HA, UA, and UA@MnFe-MOF@HA. (I) Elemental mapping of UA/siMTH1@MnFe-MOF@HA. (J) Inductively coupled plasma-optical emission spectrometry (ICP-OES) reveals the content of Fe and Mn ions in UA/siMTH1@MnFe-MOF@HA. (K, L) X-ray photoelectron spectroscopy (XPS) spectra of Fe 2p (K) and Mn 2p (L) region in UA/siMTH1@MnFe-MOF@HA. (M) X-ray diffraction (XRD) spectrum of MnFe-MOF, MnFe-MOF@HA, and UA/siMTH1@MnFe-MOF@HA. (N) The particle size distribution curves of UA/siMTH1@MnFe-MOF@HA under different conditions (phosphate-buffered saline (PBS) or 10% fetal bovine serum (FBS)). HMIM: 2-methylimidazole; FL: fluorescence intensity; a.u.: arbitrary units; Wt%: weight percentage; PDI: polydispersity index.

3.2 Properties of UA/siMTH1@MnFe-MOF@HA for CDT

Next, we investigated the *in vitro* drug release kinetics of UA/siMTH1 @MnFe-MOF@HA. UA/siMTH1@MnFe-MOF@HA remained stable in solution at pH 7.4 (physiological condition), with less than 20% release of UA or siMTH1 within 48 h. In contrast, the release of UA and siMTH1 increased dramatically at pH 5.5 (tumor environment), reaching 70% at 48 h (**Fig. 2A**). In addition, UA and siMTH1 were gradually released in the presence of GSH, with a cumulative release of 58% and 59% at 24 h, respectively. In contrast, in the absence of GSH, the release of both UA and siMTH1 was less than 20% (**Fig. 2B**). GSH levels gradually decreased with increasing concentrations of MnFe-MOF@HA nanoparticles, and this inhibitory effect was further enhanced by UA/siMTH1@MnFe-MOF@HA (**Fig. 2C**), probably because the addition of UA further depleted GSH content. To further predict the stability of nanoparticles in practical applications, we conducted decomposition experiments (**Fig. 2D**). TEM analysis showed that the structure of UA/siMTH1@MnFe-MOF@HA remained intact and uniformly dispersed after 6 h of incubation in neutral solution (pH 7.4), with only slight degradation after 12 h. In contrast, under acidic conditions (pH 5.5), the nanoparticles underwent obvious degradation with time and formed amorphous aggregates. In addition, the dissociation of nanoparticles in acidic solution released Fe and Mn ions, and EDS analysis confirmed the diffusion behavior of these ions. These results revealed that the drug release

ability of UA/siMTH1@MnFe-MOF@HA was acid/GSH dual responsive, and it may efficiently deplete GSH via redox reactions, suggesting its potential for tumor-specific therapy.

Before formally evaluating the tumor therapeutic effects of the nanoparticles, we tested their cytotoxicity and cellular uptake capacity. MnFe-MOF and MnFe-MOF@HA showed negligible toxicity to HEEC (human normal esophageal epithelial cells), even at high concentrations (200 μmol/L) (**Fig. S1A**). However, the viability of MnFe-MOF and MnFe-MOF@HA-treated Kyse-30 cells (esophageal cancer cells) exhibited a decreasing trend, showing a high concentration dependence, which was attributed to the killing effect of Fe and Mn ions on tumor cells (**Fig. 2E**). Blood compatibility is necessary to confirm the safety of nanoparticles. Compared with water (positive control group), UA/siMTH1@MnFe-MOF@HA did not cause significant damage to the erythrocyte membrane, and the hemolysis rate was less than 2.0% even at a concentration of 200 μg/mL, indicating that it has a good blood compatibility (**Fig. 2F**). These findings further support that our prepared nanoparticles can be used as potential drug delivery candidates.

Cell adhesion receptor cluster of differentiation-44 (CD44) is overexpressed in many types of cancer cells and is often utilized as HA receptor to target cancer cells [29]. Hence, in this study, we designed HA-encapsulated nanoparticles to enhance tumor targeting. UA/siMTH1@MnFe-MOF and UA/siMTH1@MnFe-MOF@HA were co-cultured with Kyse-30 cells, and the uptake of nanoparticles by the cells was observed under a fluorescence microscope. As shown in **Fig. 2G**, the nanoparticles coated with HA significantly increased the internalization of Kyse-30 cells, resulting in the strongest green fluorescence. We also found that the internalization of nanoparticles exhibited a time-dependent pattern, with uptake peaking at 6 h after induction. Furthermore, in normal cell HEEC with low CD44 expression, there was no difference in cellular uptake of nanoparticles with or without HA encapsulation (**Figs. S1B** and **S1C**). These data further suggest that the interaction between HA and CD44 confers the ability of UA/siMTH1@MnFe-MOF@HA to target cancer cells.

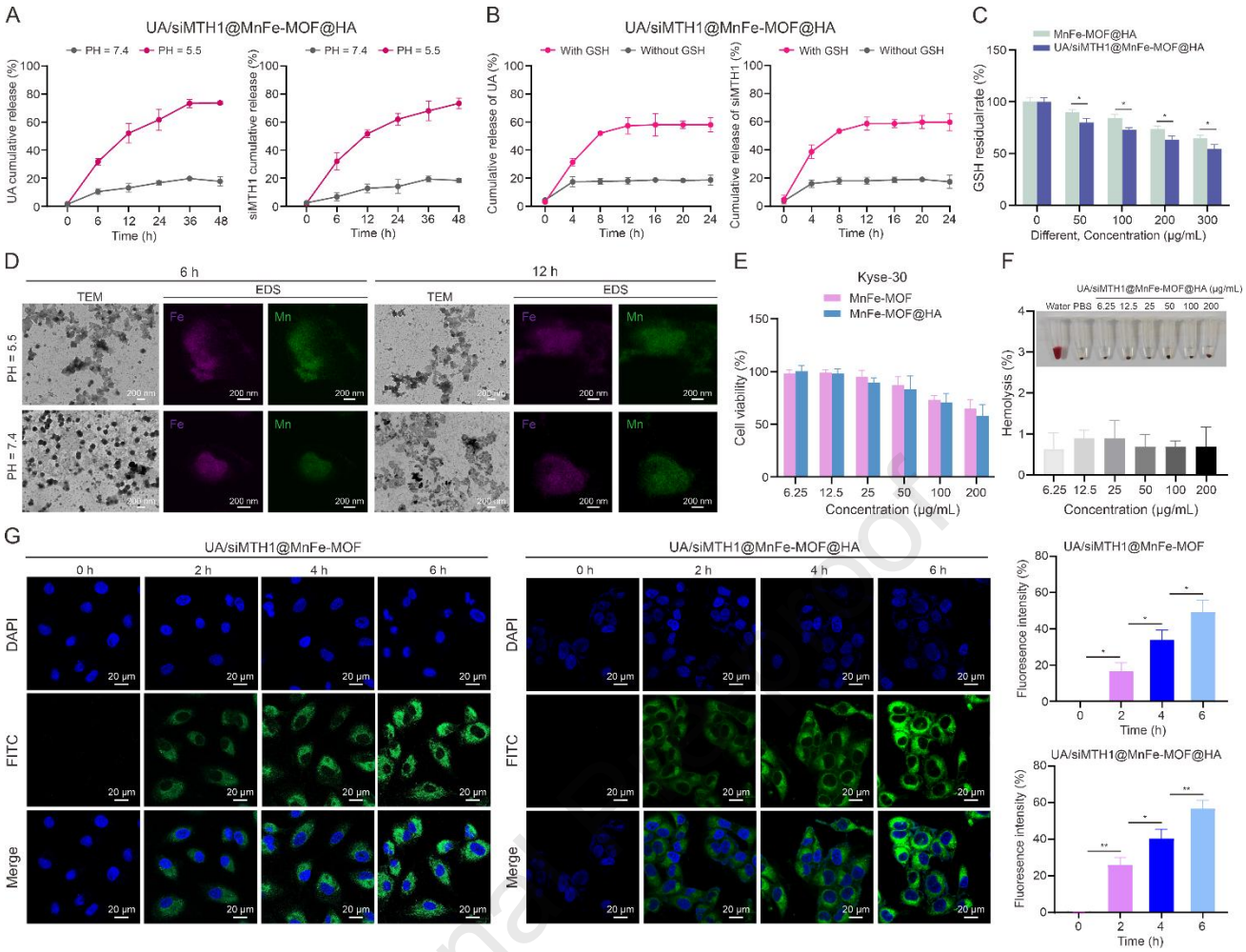

Figure 2. Drug release and intracellular phagocytosis of ursolic acid (UA)/ human MutT Homolog 1 small interfering RNA (siMTH1)@ Mn-Fe bimetallic metal-organic framework (MnFe-MOF)@ hyaluronic acid (HA). (A) Percentage release of UA and siMTH1 from UA/siMTH1@MnFe-MOF@HA over time at pH 7.4 and 5.5. (B) Release kinetics of UA and small interfering RNA (siRNA) from UA/siMTH1@MnFe-MOF@HA either in the presence or absence of 10 mm glutathione (GSH) at pH 7.4. (C) Comparison of GSH consumption of MnFe-MOF@HA and UA/siMTH1@MnFe-MOF@HA at different concentrations. (D) Transmission electron microscopy (TEM) and energy dispersive spectroscopy (EDS) images of UA/siMTH1@MnFe-MOF@HA degradation at different pH conditions (7.4 or 5.5). (E) Cell Counting Kit-8 (CCK-8) assay for cytotoxicity in Kyse-30 cells after 24 h incubation with MnFe-MOF or MnFe-MOF@HA. (F) Hemolysis rate of red blood cell after incubation with different concentrations of UA/siMTH1@MnFe-MOF@HA. (G) Confocal laser scanning microscopy (CLSM) images and quantitative analysis showing the intracellular uptake of UA/siMTH1@MnFe-MOF and UA/siMTH1@MnFe-MOF@HA by Kyse-30 cells after different incubation times. Nucleus is stained by 4',6-diamidino-2-phenylindole (DAPI, blue) and MnFe-MOF is represented by fluorescein isothiocyanate (FITC). $^{*}P < 0.05$, $^{**}P < 0.01$.

3.3 In vitro anticancer effects of UA/siMTH1@MnFe-MOF@HA

Furthermore, we determined the *in vitro* antitumor activity of the nanoparticles. CCK-8 analysis showed that cell viability decreased gradually with increasing nanoparticle concentration. Among them, UA/siMTH1@MnFe-MOF@HA exhibited the strongest inhibitory effect on cell viability, with a cell survival rate of 50% at a concentration of 50 μg/mL (**Fig. 3A**). Hence, 50 μg/mL UA/siMTH1@MnFe-MOF@HA was used as the reference concentration for the cell experiments. First, we observed the effects of drug loading and HA coating on the antitumor potential of MnFe-MOF. Compared with the control group, MnFe-MOF significantly reduced the viability of Kyse-30 cells. After loading with UA and siMTH1, the nanoparticles (UA/siMTH1@MnFe-MOF) exhibited a stronger inhibitory effect, which was attributed to the antitumor pharmacological activity of UA and the oxidative damage induced by siMTH1. Notably, HA encapsulation (UA/siMTH1@MnFe-MOF@HA) helped to enhance the cellular internalization of nanoparticles, with the most pronounced effect of cell viability inhibition induced by it (**Fig. S2A**). These findings were further confirmed by the Annexin V/PI apoptosis detection (**Figs. S2B and S2C**). The apoptosis rate induced by UA/siMTH1@MnFe-MOF@HA was much higher than that of MnFe-MOF and UA/siMTH1@MnFe-MOF.

Subsequently, Kyse-30 cells were treated with PBS, MnFe-MOF@HA, free UA, UA@MnFe-MOF@HA, and UA/siMTH1@MnFe-MOF@HA to comprehensively evaluate the cytotoxic effects of the nanoparticles. Annexin V/PI staining assay showed that UA/siMTH1@MnFe-MOF@HA significantly increased the apoptosis rate of Kyse-30 cells compared with the other groups. In addition, the apoptosis rates of UA@MnFe-MOF@HA, UA, MnFe-MOF@HA, and the blank control decreased successively (**Figs. 3B** and **C**). This result was further supported by cell cycle analysis. We found that UA/siMTH1@MnFe-MOF@HA induced a remarkable increase in the percentage of gap 1 (G1) phase cells in Kyse-30 cells, causing cell cycle arrest that contributed to a reduction in cell proliferation ability (**Figs. 3D** and **E**). Calcium AM/PI staining analysis confirmed that UA/siMTH1@MnFe-MOF@HA induced extensive Kyse-30 cell death, as indicated by red fluorescence (**Figs. 3F** and **G**). Moreover, compared to the other groups, UA/siMTH1@MnFe-MOF@HA-treated tumor cells produced the strongest green fluorescence signal (DCF-DA), indicating a large amount of ROS production (**Figs. 3H** and **I**). Overall, these findings emphasize that UA/siMTH1@MnFe-MOF@HA exerts a better role in inducing apoptosis and promoting ROS production than other nanoparticles for optimal anticancer effect.

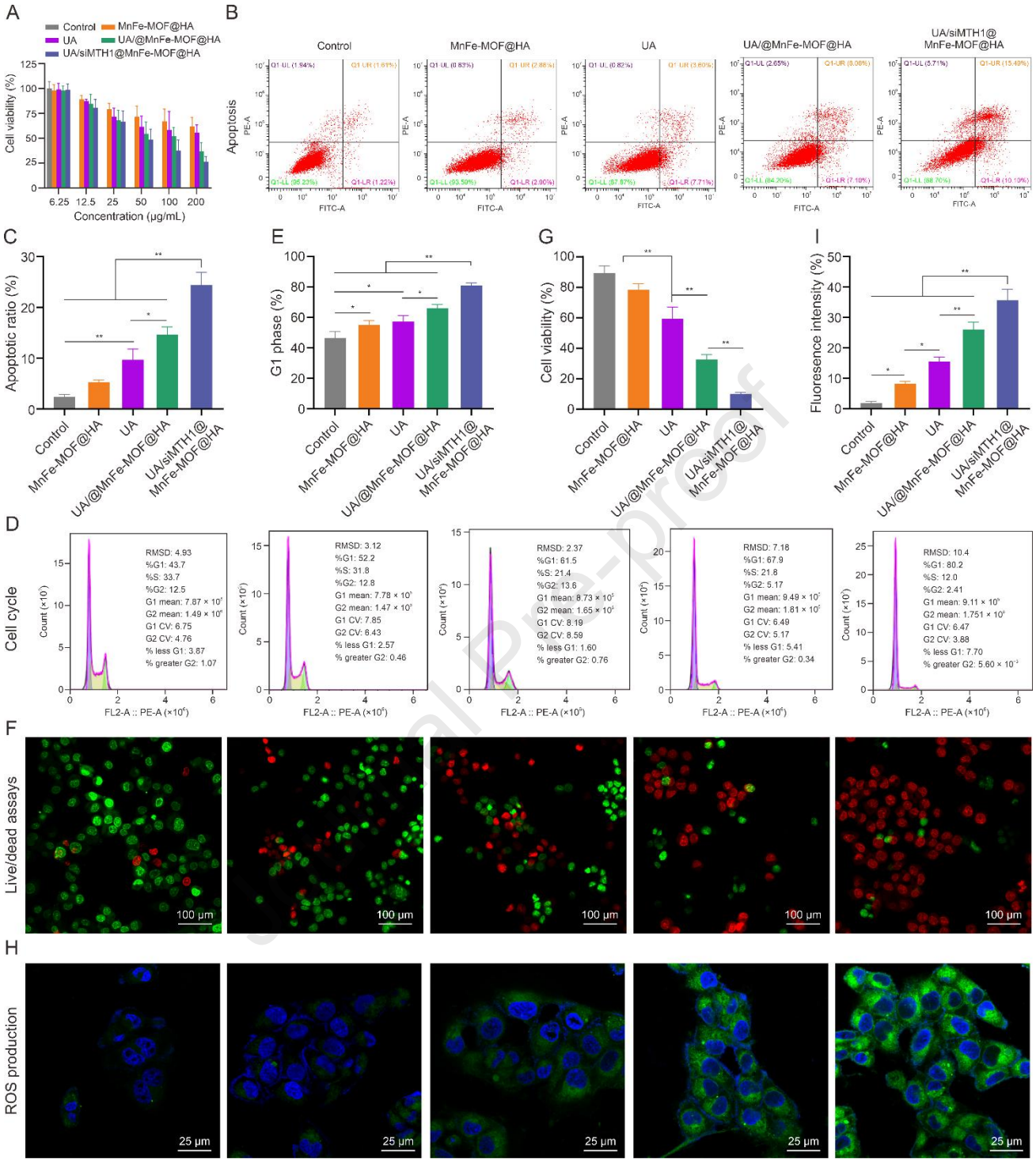

Figure 3. *In vitro* evaluation of anti-tumor efficiency of ursolic acid (UA)/ human MutT Homolog 1 small interfering RNA (siMTH1)@ Mn-Fe bimetallic metal-organic framework (MnFe-MOF)@ hyaluronic acid (HA). (A) Cell viability measured by Cell Counting Kit-8 (CCK-8) of Kyse-30 cells treated with different concentration of drugs or nanoparticles. (B) Cell apoptosis is determined by flow cytometry assay of Kyse-30 cells incubated with different treatments. (C) Quantitative results of apoptosis. (D) Cell cycle detected by flow cytometry analysis of Kyse-30 cells treated with different formulations. (E) Quantitative analysis of the number of cells in gap 1 (G1) phase. (F) Fluorescence images of calcein AM

(green, live cells) and propidium iodide (PI, red, dead cells) co-stained Kyse-30 cells after cultivation in different treatments for 24 h. (G) Quantitative results of cell viability. (H) Fluorescence images of 2′,7′-dichlorodihydrofluorescein diacetate (DCFH-DA)-stained (green, reactive oxygen species (ROS)) Kyse-30 cells exposed to different treatments. (I) Quantitative results of ROS fluorescence intensity. $^{*}P < 0.05$; $^{**}P < 0.01$. PE-A: Phycoerythrin-Area; FITC-A: Fluorescein Isothiocyanate-Area; Q1: Quadrant 1; UL: upper left; UR: upper right; LL: lower left; LR: lower right; RMSD: root-mean-square deviation; S: synthesis phase; G2: gap 2 phase; CV: coefficient of variation; FL2-A: Fluorescence 2-Area; DAPI: 4',6-diamidino-2-phenylindole.

We further explored the mechanisms underlying the anticancer effects of the nanoparticles. Previously, we found that high concentrations of GSH promoted the release of UA and siMTH1 from the nanoparticle. To comprehensively understand the impact of nanoparticles on the antioxidant ability of cancer cells, we further analyzed the intracellular levels of GSH and GSH/GSSG (**Fig. 4A**). Compared with the control group, MnFe-MOF@HA significantly inhibited the levels of GSH and GSH/GSSG in Kyse-30 cells, suggesting that Fe- and Mn-doped MOF had the ability to deplete GSH. Of interest, UA/siMTH1@MnFe-MOF@HA amplified the GSH consumption performance of MOF nanomaterial, which may be attributed to the introduction of UA and siMTH1 further aggravating the oxidative damage. Cell senescence is a permanent state of cell cycle arrest that can be caused by oxidative stress, genotoxic damage, and epigenetic changes [30]. It plays an important role in the pathophysiological process of tumor suppression. Given that UA/siMTH1@MnFe-MOF@HA nanoparticles can produce ROS and induce G1 phase arrest in cancer cells, we investigated their effect on cellular senescence. Therefore, we quantified the senescence status of the cells using SA-β-gal staining. The results showed that the percentage of SA-β-gal-positive cells was significantly enhanced in the UA/siMTH1@MnFe-MOF@HA group compared with the other groups (**Figs. 4B** and **C**). Moreover, UA/siMTH1@MnFe-MOF@HA treatment notably increased the expression of senescence-related biomarkers in Kyse-30 cells, such as TGF-β, p21, and p-Rb (**Fig. 4D**). In addition, MTH1 is a nucleic acid oxidative damage repair enzyme, and its inhibition can promote DNA damage, which in turn induces irreversible cellular senescence in cancer cells [19]. Western blot analysis confirmed that UA/siMTH1@MnFe-MOF@HA increased the expression of γH2AX in the cells. These findings demonstrate that UA/siMTH1@MnFe-MOF@HA can effectively induce cellular senescence by activating the DNA damage pathway, making it an attractive anticancer strategy.

In addition, to investigate whether siRNA could be released from the nanoparticles and effectively downregulate MTH1, western blot and RT-qPCR were performed to assess MTH1 expression using free siRNA as a control. As shown in **Figs. 4E** and **F**, nanoparticles loaded with siMTH1 (siMTH1@MnFe-MOF, siMTH1@MnFe-MOF@HA, or

459 UA/siMTH1@MnFe-MOF@HA) significantly reduced MTH1 levels in Kyse-30 cells compared to free siMTH1. Notably,
460 the expression of MTH1 remained low in UA/siMTH1@MnFe-MOF@HA treated Kyse-30 cells after three passages,
461 implying that the nanoparticles had excellent gene silencing ability (**Fig. 4G**).
462

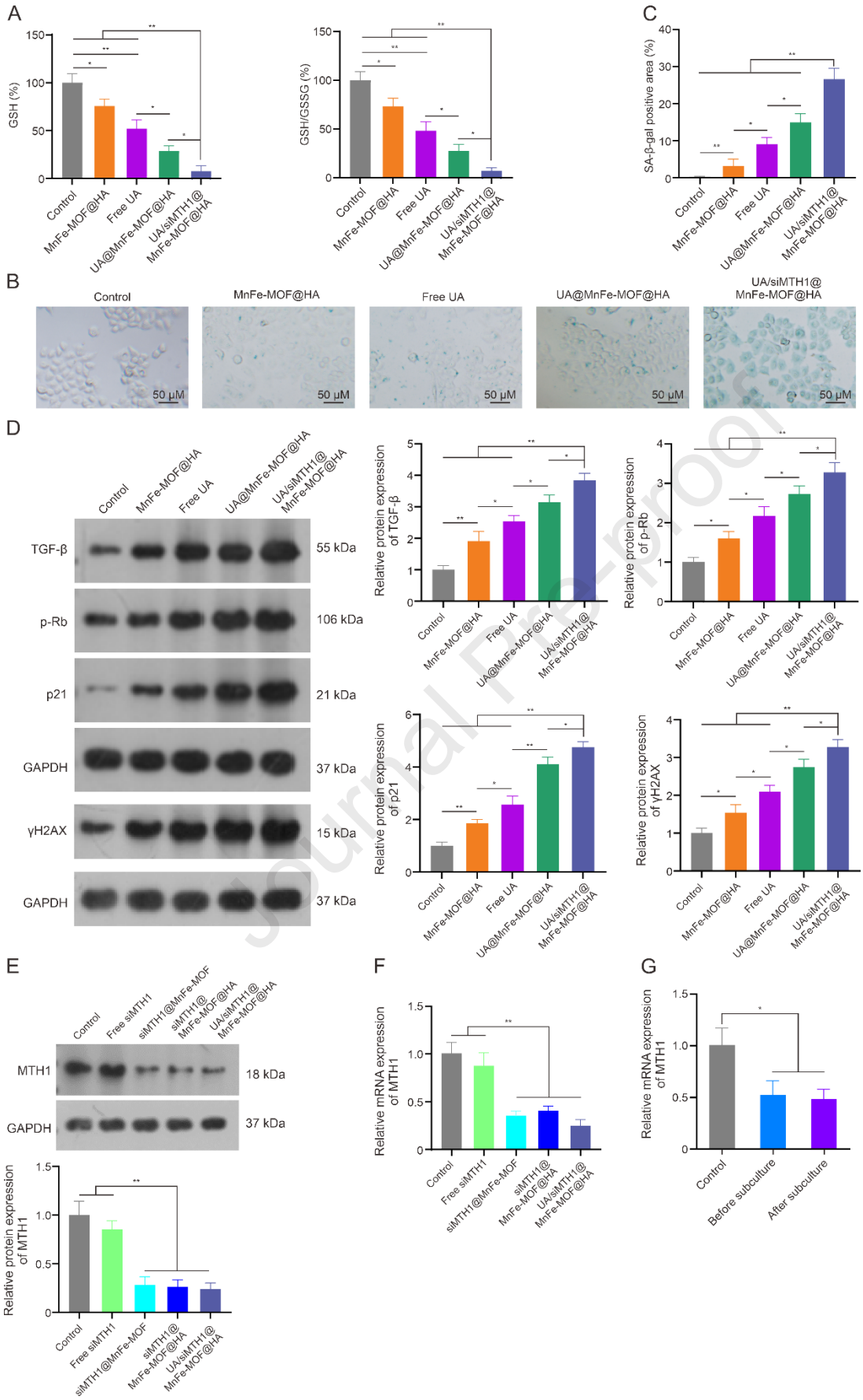

Figure 4. Mechanistic exploration of ursolic acid (UA)/ human MutT Homolog 1 small interfering RNA (siMTH1)@Mn-

Fe bimetallic metal-organic framework (MnFe-MOF)@ hyaluronic acid (HA) for anti-tumor *in vitro*. (A) Glutathione (GSH) content and GSH/glutathione disulfide (GSSG) content of Kyse-30 cells incubated with various formulations. (B, C) Representative staining images (B) and quantitative results (C) for senescence-associated-beta-galactosidase (SA-β-gal) of different preparations after 24 h incubation with Kyse-30 cells. (D) After incubation with different preparations for 24 h, the protein expression levels of transforming growth factor-beta (TGF-β), phosphorylated Retinoblastoma protein (p-Rb), p21, and gammaH2AX (γH2AX) in Kyse-30 cells were detected by western blot. (E) Immunoblotting and quantification for MTH1 protein in different groups. (F) Detection of MTH1 mRNA level in each group by reverse transcription quantitative polymerase chain reaction (RT-qPCR). (G) MTH1 mRNA level in UA/siMTH1@MnFe-MOF@HA incubated Kyse-30 cells before and after passaging was detected by RT-qPCR. $^{*}P < 0.05$; $^{**}P < 0.01$.

3.4 In vivo drug distribution studies of UA/siMTH1@MnFe-MOF@HA

Given their favorable physicochemical properties and cancer inhibition *in vitro*, we further examined the *in vivo* antitumor activity of the nanoparticles. First, we used an *in vivo* visible-light imaging system to monitor the distribution of nanoparticles *in vivo*. Kyse-30 tumor-bearing mice were intravenously injected with Cy5.5-labeled UA/siMTH1@MnFe-MOF or UA/siMTH1@MnFe-MOF@HA, followed by imaging at specific time points after injection. The fluorescence intensity at the tumor site increased with time and reached a maximum at 6 h post-injection; the fluorescence signal then gradually decayed due to metabolism. Notably, the fluorescence signal intensity in the UA/siMTH1@MnFe-MOF@HA group was higher than that in the UA/siMTH1@MnFe-MOF group, with fluorescence still detectable at the tumor site 48 h after injection (**Fig. 5A**). These findings suggest that HA encapsulation enhances the *in vivo* retention time and tumor targeting of nanoparticles. After 48 h, the mice were euthanized, and their tumor tissues and major organs were collected for *ex vivo* imaging (**Fig. 5B**). Fluorescent signals were mainly located in the tumor and liver, while distribution in other organs (heart, spleen, lung, and kidney) were negligible. The high level of signal in the liver may be attributed to the clearance of the nanoparticles by the liver. Undoubtedly, HA surface modification further enhanced the fluorescence of the nanoparticles at the tumor site. Overall, UA/siMTH1@MnFe-MOF@HA exhibited good potential for drug delivery to tumor tissues.

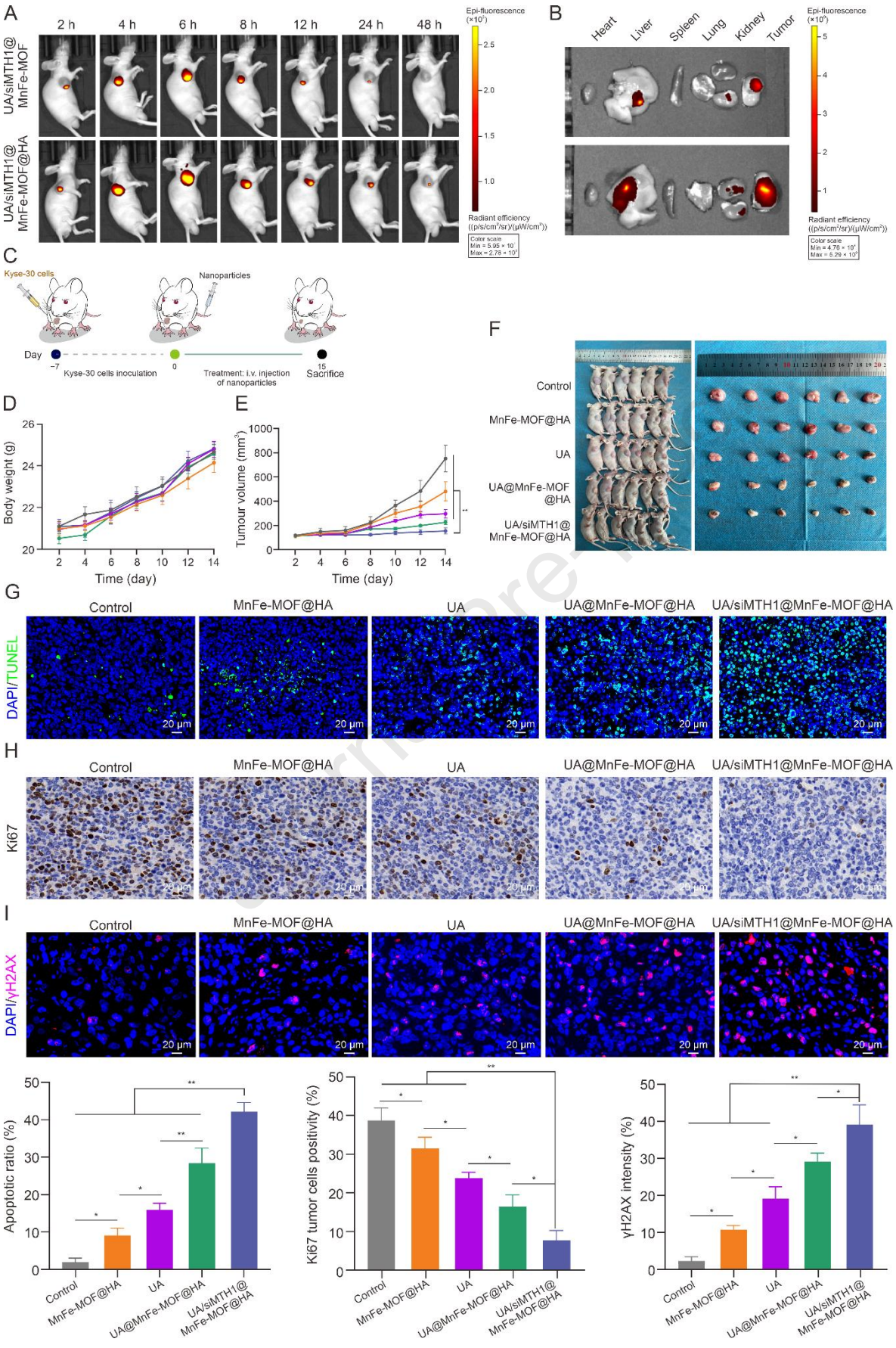

Figure 5. *In vivo* antitumor therapeutic efficacy of ursolic acid (UA)/ human MutT Homolog 1 small interfering RNA

493 (siMTH1)@ Mn-Fe bimetallic metal-organic framework (MnFe-MOF)@ hyaluronic acid (HA). (A) *In vivo* fluorescence
494 imaging of Kyse-30 tumor-bearing mice after different administration times. (B) Fluorescence intensity of major organs
495 and tumors 48 h after drug administration. (C) Schematic diagram of tumor implantation and treatment *in vivo*. (D, E) Body
496 weight (D) and tumor volume (E) curves of mice in different treatment groups. (F) Representative images of dissected
497 mice and tumors in each group after 14 days of treatment. (G–I) Terminal deoxynucleotidyl transferase dUTP nick end
498 labeling (TUNEL) (G), Ki67 (H), and gammaH2AX (γH2AX) (I) staining of tumor sections from different groups. $^{*}P <$
499 0.05; $^{**}P < 0.01$. i.v.: intravenous; DAPI: 4',6-diamidino-2-phenylindole.
500
501 ***3.5 In vivo therapeutic effects of UA/siMTH1@MnFe-MOF@HA***
502 Subsequently, experiments were conducted in Kyse-30 tumor-bearing mice to confirm the tumor ablation effect of the
503 nanoparticles *in vivo* (**Fig. 5C**). When the tumor size met the experimental requirements, PBS, MnFe-MOF@HA, UA,
504 UA@MnFe-MOF@HA, and UA/siMTH1@MnFe-MOF@HA were injected via the tail vein, and the weight changes as
505 well as tumor progression were monitored in each group during the treatment period. As shown in **Fig. 5D**, the weight of
506 the mice did not change significantly during treatment, indicating that the nanoparticles had no significant effects and did
507 not affect the normal activities of the mice. Both the free UA and nanoparticle groups exhibited varying degrees of visual
508 reduction in tumor size. In particular, the strongest tumor inhibition was observed in the UA/siMTH1@MnFe-MOF@HA
509 group (**Fig. 5E**). Images of dissected tumors at the end of treatment also confirmed this observation (**Fig. 5F**). The collected
510 tumor tissues were sectioned and stained for pathological analysis. TUNEL staining revealed that the number of apoptotic
511 cells in the UA/siMTH1@MnFe-MOF@HA group was significantly higher than that in the other treatment groups (**Fig.**
512 **5G**). Compared with the control group, all the different treatments significantly reduced Ki-67 expression in tumor tissues,
513 especially UA/siMTH1@MnFe-MOF@HA, which exerted the strongest proliferation inhibition effect (**Fig. 5H**).
514 Considering the essential role of siMTH1 in promoting DNA damage, we performed immunofluorescence staining to
515 evaluate γH2AX expression (**Fig. 5I**). The highest level of γH2AX was detected in UA/siMTH1@MnFe-MOF@HA-
516 treated mice. Taken together, UA/siMTH1@MnFe-MOF@HA had better effects on promoting apoptosis, inhibiting cell
517 proliferation, and aggravating DNA damage than the other formulations, and could effectively prevent tumor growth.
518 Consistent with the results of *in vitro* experiments, different treatments effectively induced cell senescence along with
519 cell cycle arrest, characterized by the upregulation of SA-β-gal, p21, p-Rb, and TGF-β. Similarly, the expression of these
520 indicators was highest in the UA/siMTH1@MnFe-MOF@HA group (**Figs. 6A** and **B**). In addition, compared with the other
521 groups, MTH1 expression was significantly reduced in the UA/siMTH1@MnFe-MOF@HA group, again indicating that
522 the nanoparticles had excellent MTH1 suppression ability (**Fig. 6C**). Notably, there were no obvious signs of tissue necrosis

523 in the H&E-stained sections of the major organs of the mice receiving different treatments, suggesting that the
524 nanopreparations had no obvious biotoxicity and good long-term biocompatibility *in vivo* (**Fig. 6D**). Moreover, the blood
525 biochemical indexes showed that there were no significant differences in the serum levels of ALT, AST, CRE, and Urea
526 among the groups, further indicating that the nanoparticles had good safety and did not cause obvious liver and kidney
527 toxicity (**Fig. 6E**).
528

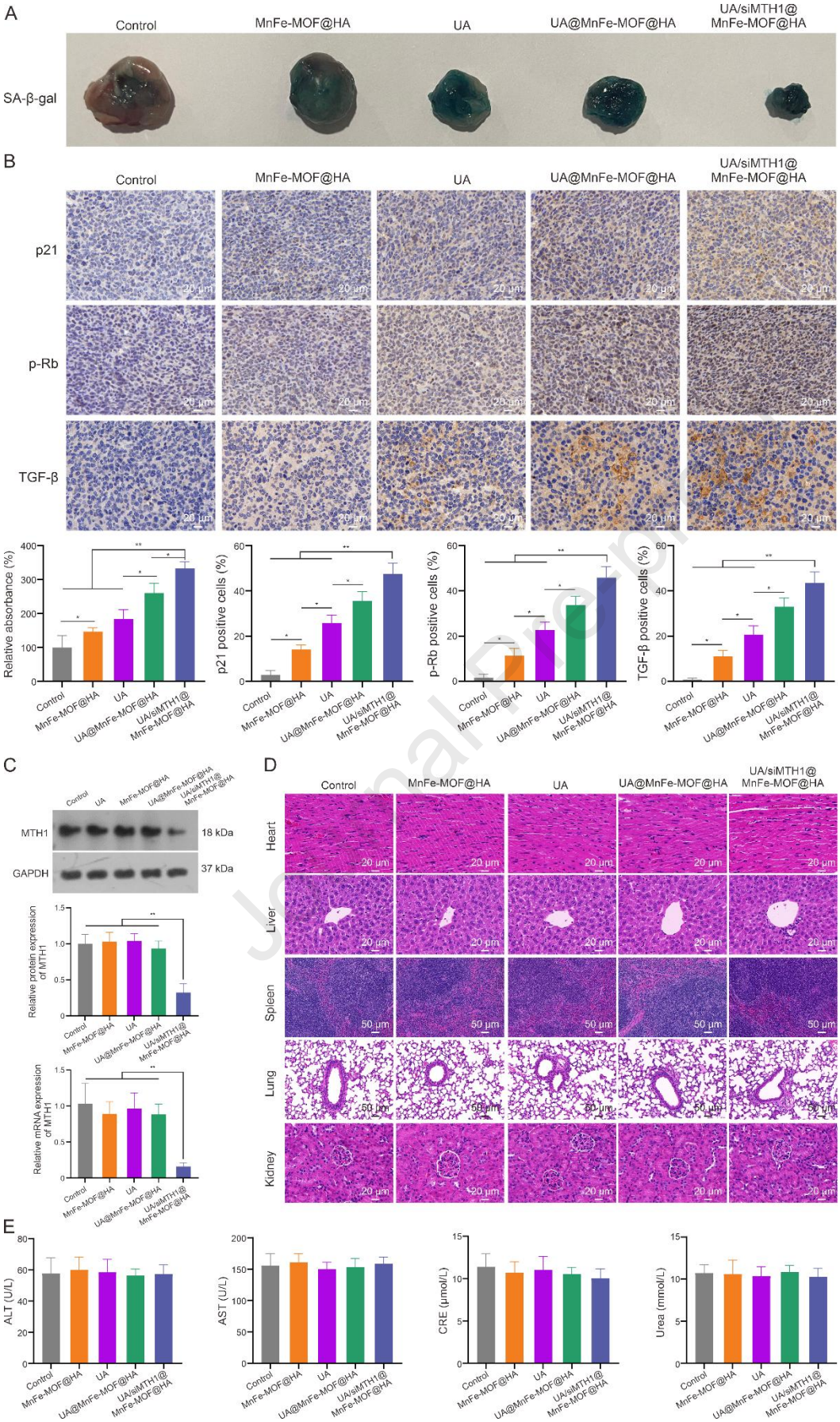

Figure 6. Investigation of anticancer mechanism and biocompatibility of ursolic acid (UA)/ human MutT Homolog 1 small

interfering RNA (siMTH1)@ Mn-Fe bimetallic metal-organic framework (MnFe-MOF)@ hyaluronic acid (HA) *in vivo.* (A) Representative images of isolated tumors stained with senescence-associated-beta-galactosidase (SA-β-gal) from each group. (B) Immunohistochemical staining (p21, phosphorylated Retinoblastoma protein (p-Rb), and transforming growth factor-beta (TGF-β)) of tumor sections from different groups. (C) Detection of MTH1 expression levels in tumor samples from different groups by western blot or reverse transcription quantitative polymerase chain reaction (RT-qPCR). (D) Hematoxylin-eosin (H&E)-stained tissue sections of major organs isolated from mice after different treatments. (E) Blood biochemistry measurements of mice after treatment with different formulations. $^{*}P < 0.05$; $^{**}P < 0.01$. ALT: aminotransferase; AST: aspartate aminotransferase; CRE: creatinine.

4. Discussion

Due to the limitations of diagnostic techniques, esophageal cancer is often detected at an advanced stage, exacerbating the tendency for metastasis and recurrence. In addition, traditional therapeutic strategies, such as surgery, radiotherapy, and chemotherapy, inevitably damage normal tissues owing to poor tumor selectivity, resulting in severe systemic toxicity [31]. Therefore, the development of targeted tumor therapies is necessary. The ideal treatment should precisely target and kill cancer cells without affecting normal cells [32]. Exploiting the differences between cancer and normal cells is a promising approach. Researchers have identified unique features of the tumor microenvironment, including weak acidity, high H_2O_2 concentrations, hypoxia, and elevated oxidative stress [33]. Numerous clinical studies have confirmed that ROS-induced therapy disrupts the redox balance of tumor cells and promotes tumor regression [34]. Notably, CDT can exploit the acidic pH and excess H_2O_2 at the tumor site. Specifically, CDT utilizes metal ions to convert H_2O_2 into harmful •OH molecules or O_2 through Fenton and Fenton-like reactions, triggering apoptosis/necrosis of cancer cells [35]. In addition, insufficient H_2O_2 and alkaline conditions in the normal tissue microenvironment greatly limit the progress of Fenton and similar reactions [36]. Collectively, CDT plays a key role in the selective clearance of cancer cells and has attracted increasing interest from the medical and scientific communities. More importantly, when CDT is combined with the advantages of nanomedicine, it becomes a more effective and powerful tool for cancer treatment [37]. Based on these facts, we designed a nanoparticle called UA/siMTH1@MnFe-MOF@HA, consisting of a MOF nanoframework doped with Fe and Mn ions, biomedicine UA and siMTH1, and a surface HA coating, to achieve targeted therapy for esophageal cancer.

In this study, we systematically evaluated the inhibitory effects of UA/siMTH1@MnFe-MOF@HA on esophageal cancer. The main findings were as follows: 1) UA/siMTH1@MnFe-MOF@HA dramatically promoted apoptosis and G1 phase arrest in Kyse-30 cells while inhibiting cell proliferation. 2) UA combined with siMTH1 triggered DNA damage and induced cellular senescence, thereby impairing cancer cell growth. 3) UA/siMTH1@MnFe-MOF@HA maintained stable

body weight in tumor-bearing nude mice and significantly reduced tumor volume. 4) UA/siMTH1@MnFe-MOF@HA-treated mice showed no obvious signs of tissue necrosis in the HE-stained sections of the major organs, and did not cause significant hepatic and nephrotoxicity, suggesting excellent biosafety and biocompatibility. 5) Mechanistic explorations revealed that the specific tumor microenvironment (low pH and high GSH level) promoted the Fenton reaction of Fe and Mn ions in the nanoparticles to achieve efficient ROS production. Meanwhile, the enrichment of metal ions depleted GSH, which helped to reduce ROS clearance and increased oxidative stress levels in cells, further synergizing the drug to kill tumor cells. These findings provide compelling evidence to support the powerful antitumor properties of synthetic UA/siMTH1@MnFe-MOF@HA.

The MOF framework has been widely used to deliver ions, phytochemicals, and antigens because of its unique structure, easy functionalization, and large surface area. However, most MOFs have limited anticancer activity, and a large number of drug-carrying MOFs may lead to potential metal and ligand toxicity [38]. To this end, nanocarriers with intrinsic anticancer activity, such as excess-ion-based MOFs, have been fabricated to overcome the challenges faced by MOFs in tumor treatment. For example, MOF-based nanoplatforms efficiently loaded with metal ions (e.g., Mn^{2+}, Fe^{2+}, and Cu^{2+}) can produce metal ions through self-degradation and enhance the effect of CDT on tumors by increasing the H_2O_2 content at the tumor site [39]. In addition, metal ions in MOF can confer GSH-consuming and catalytic properties to the MOF nanoframework, further inducing tumor apoptosis and realizing efficient cancer therapy [40]. This nanoplatform facilitates both ROS generation and GSH depletion, making it an ideal candidate for CDT. A previous study found that Fe^{2+}/Mn^{2+} ions doped in nanostructures triggered the Fenton reaction in the presence of H_2O_2, while interfering with the lipid peroxidative response to consume GSH, thus producing a long-lasting antitumor response [41]. This finding is consistent with our findings. In the design of nanoparticles, we used HA for surface modification. Its incorporation can target the highly expressed CD44 receptor on the tumor cell membrane and enhance the uptake of nanoparticles by tumor cells through receptor-mediated internalization [42]. This was also confirmed by us. HA encapsulation could greatly promote the internalization of nanoparticles by cancer cells (Kyse-30), whereas the uptake of nanoparticles by normal cells (HEEC) was limited and unaffected by HA. Next, UA and siMTH1 were loaded into the MnFe-MOF@HA nanocarriers as therapeutic agents. As expected, the anticancer activity of UA combined with the pro-DNA damage properties of siMTH1 achieved an inhibitory effect on esophageal cancer, which further synergized with CDT to effectively ablate tumor cells and produce excellent antitumor efficacy. Ren et al. [43] constructed an HTCG@TA nanoplatform that could amplify the damage of ROS to tumor cells by combining MTHI inhibitor and CDT, resulting in a promising anticancer effect *in vivo* and *in vitro*. This further supports the reliability of our findings. Notably, the constructed UA/siMTH1@MnFe-MOF@HA was strongly stabilized under physiological conditions and degraded only in cancerous environments, which is

advantageous for precision-targeted therapy.

We successfully designed and synthesized a bimetallic-doped MOF nanocomposite drug for precision tumor treatment through monotherapy. Although UA/siMTH1@MnFe-MOF@HA nanoparticles showed obvious advantages in cancer therapy, they still face significant challenges in practical clinical applications. For example, the biosafety of MOF-based nanoplatforms is a key issue that must be carefully emphasized in cancer treatment [44]. In this study, we focused on exploring the short-term toxicity of nanomaterials, ignoring their long-term toxicity, which limits the wide application of MOF nanoplatforms in cancer treatment. In addition, the stability and premature removal of MOF-based nanoplatforms during cycling are also issues of concern. Although we observed the stability of nanoparticles in a simulated physiological environment, the complexity of the natural biological environment must be considered [45]. In future research, we will investigate the degradation pathway and metabolic mechanism of UA/siMTH1@MnFe-MOF@HA *in vivo*, which will provide theoretical support for the precise dosage and administration frequency of nanomedicines in tumor therapy.

5. Conclusions

Overall, we synthesized a nanoparticle named UA/siMTH1@MnFe-MOF@HA for the efficient delivery of metal ions, AU, and siMTH1, which exhibited smart responsiveness to specific signals in the tumor microenvironment. Specifically, HA endowed the nanoparticles with active targeting ability and facilitated slow drug release. In the specific microenvironment of the tumor, UA/siMTH1@MnFe-MOF@HA dissociates into Mn and Fe ions for a Fenton or Fenton-like reaction to generate ROS and efficiently scavenges GSH, while releasing UA and siMTH1 to exacerbate tumor cell apoptosis. Moreover, siMTH1 released from nanoparticles hindered DNA repair function, leading to the amplification of intracellular oxidative damage. UA arrested cancer cells in the G1 phase and further inhibited cancer cell proliferation. Notably, UA/siMTH1@MnFe-MOF@HA exhibited satisfactory biosafety, making it a promising candidate for clinical translation. This combined CDT/gene therapy strategy addresses the problems of H_2O_2 deficiency, pH dependence, and high GSH levels in CDT, providing a new avenue to improve future anticancer efficacy.

References

[1] F. Bray, M. Laversanne, H. Sung, et al., Global cancer statistics 2022: GLOBOCAN estimates of incidence and mortality worldwide for 36 cancers in 185 countries, CA Cancer J. Clin. 74 (2024) 229–263.

[2] H. Qu, Q. Li, L. Hao, et al., Esophageal cancer screening, early detection and treatment: Current insights and future directions, World J. Gastrointest. Oncol. 16 (2024) 1180–1191.

[3] Y. Zhang, Y. Zhang, L. Peng, et al., Research progress on the predicting factors and coping strategies for postoperative

recurrence of esophageal cancer, Cells 12 (2022), 114.

[4] S. Jäger, H. Trojan, T. Kopp, et al., Pentacyclic triterpene distribution in various plants–rich sources for a new group of multi-potent plant extracts, Molecules 14 (2009) 2016–2031.

[5] M. Zhao, F. Wu, Z. Tang, et al., Anti-inflammatory and antioxidant activity of ursolic acid: A systematic review and meta-analysis, Front Pharmacol. 14 (2023), 1256946.

[6] S. Fontanay, M. Grare, J. Mayer, et al., Ursolic, oleanolic and betulinic acids: Antibacterial spectra and selectivity indexes, J. Ethnopharmacol. 120 (2008) 272–276.

[7] M. Luan, H. Wang, J. Wang, et al., Advances in anti-inflammatory activity, mechanism and therapeutic application of ursolic acid, Mini Rev. Med. Chem. 22 (2022) 422–436.

[8] Y. Limami, A. Pinon, H. Wahnou, et al., Ursolic acid's alluring journey: One triterpenoid vs. cancer hallmarks, Molecules 28 (2023), 7897.

[9] S. Zafar, K. Khan, A. Hafeez, et al., Ursolic acid: A natural modulator of signaling networks in different cancers, Cancer Cell Int. 22 (2022), 399.

[10] J. Zou, J. Lin, C. Li, et al., Ursolic acid in cancer treatment and metastatic chemoprevention: From synthesized derivatives to nanoformulations in preclinical studies, Curr. Cancer Drug Targets 19 (2019) 245–256.

[11] D. Yu, Z. Kan, F. Shan, et al., Triple strategies to improve oral bioavailability by fabricating coamorphous forms of ursolic acid with piperine: Enhancing water-solubility, permeability, and inhibiting cytochrome P450 isozymes, Mol. Pharm. 17 (2020) 4443–4462.

[12] S. Biswas, P.K. Mukherjee, R.K. Harwansh, et al., Enhanced bioavailability and hepatoprotectivity of optimized ursolic acid-phospholipid complex, Drug Dev. Ind. Pharm. 45 (2019) 946–958.

[13] Q. Sun, M. He, M. Zhang, et al., Ursolic acid: A systematic review of its pharmacology, toxicity and rethink on its pharmacokinetics based on PK-PD model, Fitoterapia. 147 (2020), 104735.

[14] L. Wang, Q. Yin, C. Liu, et al., Nanoformulations of ursolic acid: A modern natural anticancer molecule, Front. Pharmacol. 12 (2021), 706121.

[15] Y. Yang, P. Hong, W. Xu, et al., Advances in targeted therapy for esophageal cancer, Signal Transduct. Target. Ther. 5 (2020), 229.

[16] J.E. Rogers, M. Sewastjanow-Silva, R.E. Waters, et al., Esophageal cancer: Emerging therapeutics, Expert Opin. Ther. Targets 26 (2022) 107–117.

[17] Y. Rose Li, K.D. Halliwill, C.J. Adams, et al., Mutational signatures in tumours induced by high and low energy radiation in Trp53 deficient mice, Nat. Commun. 11 (2020), 394.

[18] Y. Wang, H. Qi, Y. Liu, et al., The double-edged roles of ROS in cancer prevention and therapy, Theranostics 11 (2021) 4839–4857.

[19] A. Taiyab, A. Ashraf, M.N. Sulaimani, et al., Role of MTH1 in oxidative stress and therapeutic targeting of cancer, Redox Biol. 77 (2024), 103394.

[20] H. Gad, T. Koolmeister, A.-S. Jemth, et al., MTH1 inhibition eradicates cancer by preventing sanitation of the dNTP pool, Nature 508 (2014) 215–221.

[21] S. Akiyama, H. Saeki, Y. Nakashima, et al., Prognostic impact of MutT homolog-1 expression on esophageal squamous cell carcinoma, Cancer Med. 6 (2017) 258–266.

[22] G. Raj, D.S. Vasudev, S. Christopher, et al., Multifunctional siRNA/ferrocene/cyclodextrin nanoparticles for enhanced chemodynamic cancer therapy, Nanoscale 16 (2024) 3755–3763.

[23] D. Deng, Y. Wang, S. Wen, et al., Metal-organic framework composite Mn/Fe-MOF@Pd with peroxidase-like activities for sensitive colorimetric detection of hydroquinone, Anal. Chim. Acta 1279 (2023), 341797.

[24] Q. Ouyang, Y. Zhao, K. Xu, et al., Hyaluronic acid receptor-mediated nanomedicines and targeted therapy, Small Methods 8 (2024), e2400513.

[25] J. Shi, W. Ma, J. Deng, et al., Self-assembled hyaluronic acid nanomicelle for enhanced cascade cancer chemotherapy via self-sensitized ferroptosis, Carbohydr. Polym. 343 (2024), 122489.

[26] B. Ghaemi, M. Javad Hajipour, Tumor acidic environment directs nanoparticle impacts on cancer cells, J. Colloid Interface Sci. 634 (2023) 684–692.

[27] X. Kong, Q. Chen, G. Wan, et al., Hyaluronic acid-enwrapped polyoxometalate complex for synergistic near infrared-II photothermal/chemo-therapy and chemodynamic therapy, Biomacromolecules 23 (2022) 3752–3765.

[28] P. Janjani, U. Bhardwaj, R. Gupta, et al., Bimetallic Mn/Fe MOF modified screen-printed electrodes for non-enzymatic electrochemical sensing of organophosphate, Anal. Chim. Acta 1202 (2022), 339676.

[29] E. Pashkina, M. Bykova, M. Berishvili, et al., Hyaluronic acid-based drug delivery systems for cancer therapy, Cells 14 (2025), 61.

[30] L. Zhang, L.E. Pitcher, M.J. Yousefzadeh, et al., Cellular senescence: A key therapeutic target in aging and diseases, J. Clin. Invest. 132 (2022), e158450.

[31] B. Liu, H. Zhou, L. Tan, et al., Exploring treatment options in cancer: Tumor treatment strategies, Signal Transduct. Target. Ther. 9 (2024), 175.

[32] D. Karati, D. Kumar, A comprehensive review on targeted cancer therapy: New face of treatment approach, Curr. Pharm. Des. 29 (2023) 3282–3294.

[33] M. Zhang, X. Guo, M. Wang, et al., Tumor microenvironment-induced structure changing drug/gene delivery system for overcoming delivery-associated challenges, J. Control. Release 323 (2020) 203–224.

[34] B. Niu, K. Liao, Y. Zhou, et al., Application of glutathione depletion in cancer therapy: Enhanced ROS-based therapy, ferroptosis, and chemotherapy, Biomaterials 277 (2021), 121110.

[35] J. Xin, C. Deng, O. Aras, et al., Chemodynamic nanomaterials for cancer theranostics, J. Nanobiotechnology 19 (2021), 192.

[36] R. Ou, G. Aodeng, J. Ai, Advancements in the application of the Fenton reaction in the cancer microenvironment, Pharmaceutics 15 (2023), 2337.

[37] W. Ahmad, W. Sajjad, Q. Zhou, et al., Nanomedicine for combination of chemodynamic therapy and immunotherapy of cancers, Biomater. Sci. 12 (2024) 4607–4629.

[38] Q. Zhang, S. Yan, X. Yan, et al., Recent advances in metal-organic frameworks: Synthesis, application and toxicity, Sci. Total Environ. 902 (2023), 165944.

[39] J. Cun, X. Fan, Q. Pan, et al., Copper-based metal-organic frameworks for biomedical applications, Adv. Colloid Interface Sci. 305 (2022), 102686.

[40] J. Yang, D. Dai, X. Zhang, et al., Multifunctional metal-organic framework (MOF)-based nanoplatforms for cancer therapy: From single to combination therapy, Theranostics 13 (2023) 295–323.

[41] Z. Hu, X. Song, L. Ding, et al., Engineering Fe/Mn-doped zinc oxide nanosonosensitizers for ultrasound-activated and multiple ferroptosis-augmented nanodynamic tumor suppression, Mater. Today Bio 16 (2022), 100452.

[42] J. Chandra, N. Molugulu, S. Annadurai, et al., Hyaluronic acid-functionalized lipoplexes and polyplexes as emerging nanocarriers for receptor-targeted cancer therapy, Environ. Res. 233 (2023), 116506.

[43] C. Ren, Z. Shi, X. Zhang, et al., DNA-mediated self-assembly oxidative damage amplifier combined with copper and MTH1 inhibitor for cancer therapy, Bioact. Mater. 45 (2025) 434–445.

[44] X. Huang, X. Sun, W. Wang, et al., Nanoscale metal-organic frameworks for tumor phototherapy, J. Mater. Chem. B 9 (2021) 3756–3777.

[45] S.E. Alavi, S. Alharthi, S.Z. Alavi, et al., Bioresponsive drug delivery systems, Drug Discov. Today 29 (2024), 103849.

Availability of data and material

The datasets used and/or analyzed in the current study are available from the corresponding author upon reasonable request.

Acknowledgments

We would like to thank The Fourth Affiliated Hospital of China Medical University, The Shengjing Hospital of China Medical University, Shandong First Medical University and Shandong Academy of Medical Sciences, NOVA Medical School, and Yangzhou University for providing a research platform, which laid the foundation for the smooth progress of the project.

Author' contribution

Jia Ma: Conceptualization, Investigation, Software, Data curation, Writing - original draft. **Xin Zhang:** Conceptualization, Data curation, Formal analysis, Writing - original draft. **Xiangpeng Meng:** Project administration, Investigation, Formal analysis, Visualization. **Yuhang Dai:** Data curation, Formal analysis, Visualization. **Huaiyong Wang:** Formal analysis, Software. **João Conde:** Investigation, Formal analysis, Writing - original draft. Writing - review and editing. **Zhenggang Li:** Project administration, Investigation, Formal analysis, Writing - original draft. **Enyang Yao:** Project administration, Investigation, Visualization, Writing - review and editing. **Wei He:** Conceptualization, Data curation, Formal analysis, Writing - review and editing.

Highlights

1. Mn/Fe bimetallic doped MOF nanoplatforms were constructed for co-delivery of UA and MTH1 siRNA, followed by coating with HA.

2. UA/siMTH1@MnFe-MOF@HA induced cancer cell death via depleting GSH, enhancing ROS production and promoting DNA damage.

3. UA/siMTH1@MnFe-MOF@HA exhibited high biosafety in vivo.

Declaration of Interest Statement

João Conde is a co-founder and shareholder of TargTex S.A. - targeted therapeutics for Glioblastoma Multiforme. João Conde is also a member of the Global Burden Disease (GBD) consortium of the Institute for Health Metrics and Evaluation (IHME), University of Washington (US). The other authors declare that there are no conflicts of interest.